Volume 12 | Number 7 | 7 April 2025

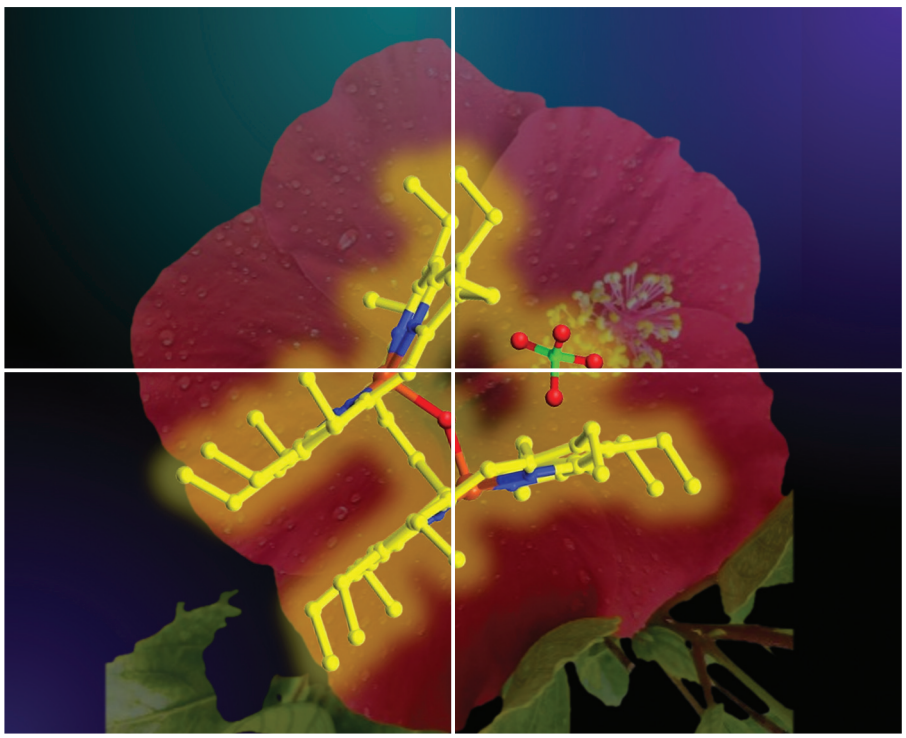

INORGANIC CHEMISTRY

FRONTIERS

CCS 中国化学会 CHINESE CHEMICAL SOCIETY

PEKING UNIVERSITY 1898

ROYAL SOCIETY OF CHEMISTRY

rsc.li/frontiers-inorganic

INORGANIC CHEMISTRY FRONTIERS

RESEARCH ARTICLE

View Article Online
View Journal | View Issue

Cite this: *Inorg. Chem. Front.*, 2025, **12**, 2613

Modulating magnetic exchange, spin dynamics and intermacrocyclic interactions *via* an oxo-bridge in dihemes through stepwise oxidations†‡

Sayantani Banerjee,[a] Rupesh Kumar Tiwari,[b] Paulami Chakraborty,[a] Gopalan Rajaraman *[b] and Sankar Prasad Rath *[a]

A bis-Fe(III)-μ-oxo-porphyrin dimer, where a rigid ethene linker covalently connects the two porphyrin units, has been exploited to investigate the effect of intermacrocyclic interactions and spin coupling upon stepwise oxidations. The complex possesses a bent Fe–O–Fe unit bringing two porphyrin macrocycles into close vicinity, which results in strong intermacrocyclic interactions between them. Here, the two high-spin iron(III) centres undergo strong anti-ferromagnetic coupling *via* the oxo-bridge (J_{Fe-Fe}), resulting in a large upfield shift of the protons in the diamagnetic region of its ^{1}H NMR spectrum. 1e$^-$-oxidation produces a porphyrin π-cation radical that displays a well-resolved ^{1}H NMR spectrum with large isotropic shifts of the downfield-shifted methylene protons, indicative of much weaker anti-ferromagnetic coupling *via* the oxo bridge. As observed in the X-ray structure of the complex, 1e$^-$-oxidation brings two porphyrin macrocycles much closer to each other. This results in a remarkably bent Fe–O–Fe unit that causes the porphyrin cores to become much more distorted due to stronger intermacrocyclic interactions between them. In addition, the Fe–N_{por} and Fe–O distances are also significantly decreased and increased, respectively, in the 1e$^-$-oxidized complex as compared with the unoxidized one, causing a significant decrease in the J_{Fe-Fe} value. The di-cation di-radical complex that results from 2e$^-$-oxidation, on the other hand, exhibits a weakly paramagnetic nature with significant upfield shifts of the methylene proton signals as well as smaller isotropic shifts than its 1e$^-$-oxidized complex. This suggests that the former has a much stronger anti-ferromagnetic coupling (J_{Fe-Fe}) *via* the oxo group compared to the 1e$^-$-oxidized complex. Most interestingly, the ^{1}H NMR chemical shift of the methylene protons of the 1e$^-$- and 2e$^-$-oxidized complexes behave completely differently upon varying the temperature and follow Curie and anti-Curie behavior, respectively, which has been rationalized by considering the thermal population of the ground and excited states at the recorded temperatures. Variable temperature magnetic investigation in the solid state indicated antiferromagnetic coupling between the iron centres through the oxo bridge, which follows the order (J_{Fe-Fe}): oxo-bridged dimer (–130.4 cm^{-1}) > 2e$^-$-oxidized complex (–116.1 cm^{-1}) ≫ 1e$^-$-oxidized complex (–37.8 cm^{-1}). On the other hand, the spin couplings between unpaired iron spin with porphyrin π-cation radical (J_{Fe-r}) are also antiferromagnetic but with relatively smaller values with an order: 2e$^-$-oxidized complex (–27.2 cm^{-1}) > 1e$^-$-oxidized complex (–16.5 cm^{-1}). The DFT calculations not only reproduce the experimental *J* values very well but also provide an insight that suggests both the Fe–O–Fe angle and the Fe–O distances determine the overall *J* value while the bridging ethylene linker promotes ferromagnetic coupling.

Received 21st November 2024,
Accepted 11th December 2024

DOI: 10.1039/d4qi02972k

rsc.li/frontiers-inorganic

[a]*Department of Chemistry, Indian Institute of Technology Kanpur, Kanpur – 208016, India. E-mail: sprath@iitk.ac.in*
[b]*Department of Chemistry, Indian Institute of Technology Bombay, Mumbai – 400076, India. E-mail: rajaraman@chem.iitb.ac.in*

† Dedicated to Professor Amitava Das on the occasion of his 65th birthday.

‡ Electronic supplementary information (ESI) available: Text, figures, and tables depicting detailed experimental procedures and characterisation data including UV-vis, X-ray crystallography and DFT calculations. CCDC 2377591. For ESI and crystallographic data in CIF or other electronic format see DOI: https://doi.org/10.1039/d4qi02972k

Introduction

Oxo- and hydroxo-bridged diiron cores are very common structural units found to play a significant role in the functioning of a large number of proteins and enzymes *viz.* O_2 metabolism in hemerythrin, methane monooxygenase (MMOH), ribonucleotide reductases (RNRR2), fatty acid desaturases, *etc.*[1–6] Also, the dioxygen activations are often modulated by diiron

centres in which the transformation between the oxo and hydroxo group is either a mandatory or proposed step in the reaction pathways.[1–6] For example, the bacterial multicomponent monooxygenase, more precisely its soluble methane analogue (sMMO), contains oxo- and hydroxo-bridged diiron active centres and is responsible for many different biochemical O_2 utilization pathways including conversion of methane to methanol. Apart from these examples, ferritins are iron-storage proteins containing μ-oxo/hydroxo diiron(III) units. The highly versatile oxo/hydroxo-bridged bimetallic core enables the control of a variety of properties for intermediates in catalytic cycles.

Cofacial 'Pacman'-type diheme-centres provide molecular cleft for the binding and activation of a variety of small molecules (*e.g.*, O_2, N_2, CO_2 and H_2).[7,8] The cooperative interaction between two heme units plays a significant role in exerting these functions.[7–13] The chemical and electrochemical nature of the Fe–O–Fe/Fe–O(H)–Fe unit is suitably controlled by the intermacrocyclic interaction between two heme centres thereby influencing the structure, property, and reactivity of the molecule to a large extent. We have earlier reported a series of μ-oxo and μ-hydroxo complexes of ethane- and ethene-bridged diiron(III) porphyrin dimers and their structures, properties, and photo-catalytic activities have also been studied to expand the use of these molecules for catalytic multi-electron reactivity and small-molecule activation.[11–13] Structurally, Fe–O–Fe units tend towards linearity because of π-bonding and steric effects.[13] The 1,2-ethene-bridged porphyrin dimer can influence the interporphyrin distance and angles due to its vertical flexibility for possible modulation of its structure and property.[13] In the present work, the bis-Fe(III)-μ-oxo complex of such a porphyrin dimer has been utilized for modulating spin coupling through the oxo-bridge along with the structural change of the Fe–O–Fe unit upon stepwise oxidations.

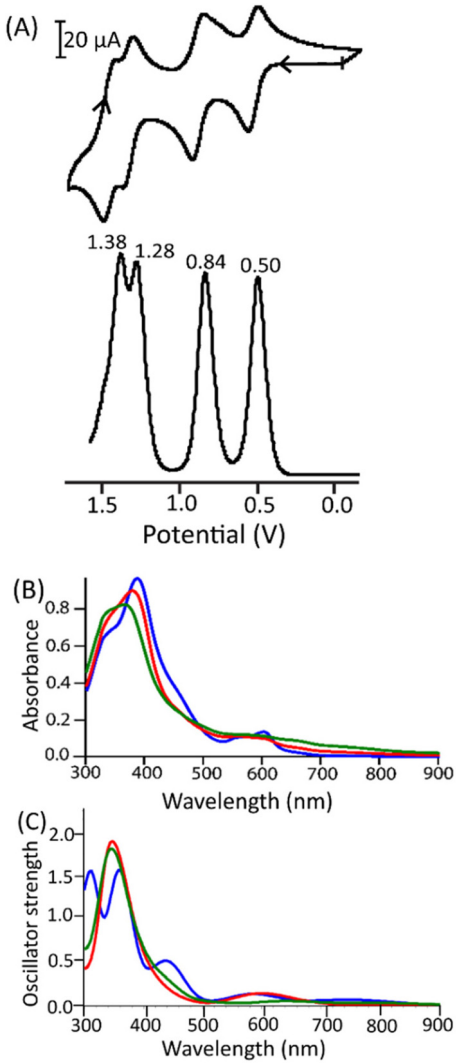

Fig. 1 (A) Cyclic voltammogram (top) and DPV (bottom) of **P2** in CH_2Cl_2 at 295 K (scan rate 100 mV s^{-1}) with 0.1 M tetra(*n*-butyl) ammonium perchlorate as supporting electrolyte. The reference electrode is Ag/AgCl. (B) UV-visible spectra of **P2** (blue line), **P3** (red line), and **P4** (green line) in dichloromethane at 295 K. (C) UV-visible spectra in CH_2Cl_2 computed from TD-DFT calculations at the CAM-B3LYP/6-31G*/LANL2DZ level of theory for **P2** (blue line), **P3** (red line) and **P4** (green line).

Results and discussion

Cis-1,2-bis[chloroiron(III)5-(2,3,7,8,12,13,17,18-octaethylporphyrinyl)]ethene, **P1**[14] and *cis*-1,2-bis[μ-oxo iron(III)5-(2,3,7,8,12,13,17,18-octaethylporphyrinyl)]ethene, **P2** have been synthesized as reported previously.[13] A dichloromethane solution of **P1**, after shaking with 5% NaOH solution, is instantly converted to diiron(III)-μ-oxo-porphyrin dimer **P2**, which is found to be green in colour and has been isolated in pure form after chromatographic separation in basic alumina using dichloromethane as the eluent in excellent yield. The UV-visible spectrum of **P1** in dichloromethane shows an intense Soret band at 375 nm whereas, for **P2**, the Soret band is shifted to 394 nm along with two Q-bands at 556 and 600 nm.[13]

Cyclic voltammetry of **P2** at 295 K in CH_2Cl_2 reveals four reversible/quasi-reversible one-electron oxidations at 0.50, 0.84, 1.28 and 1.38 V (Fig. 1A).[13] The monomeric analog $[Fe(OEP)]_2O$, however, has been found to have similar oxidations at relatively higher potentials of 0.65, 0.93, 1.30 and 1.54 V.[13] It is indeed interesting to investigate how the electronic structure and spin coupling behavior of the μ-oxo dimer changes upon stepwise oxidations since electronic communications may be involved *via* the oxo-bridge, or *via* the ethene-bridge or *via* both.

The coulometric oxidation of **P2** has been performed in dichloromethane by applying a constant potential of 0.70 V (Fig. S1A‡), which resulted in a change in colour from green to brown due to the formation of one electron-oxidized species, **P3**. The UV-visible spectrum of **P3** is indicative of porphyrin π-cation radical formation: the intensity of the Soret band at

383 nm gradually decreases upon oxidation along with a blue shift with respect to that of the neutral μ-oxo complex, **P2**, that appears at 394 nm. The blue shift of the Soret band reflects the further closeness of the two porphyrin rings in the oxidized product **P3** leading to an increased intermacrocyclic interaction. However, oxidation of **P2** at 1.04 V (Fig. S1B‡) formed a red solution due to the formation of $2e^-$-oxidized species, **P4**. The Soret band and Q-band appear at 376 nm and 575 nm, respectively, for complex **P4**. Fig. 1B compares the UV-visible spectra of **P2**, **P3**, and **P4**. It is also interesting to note here that the addition of 5% $HClO_4$ to the μ-oxo porphyrin dimer, **P2**, produces an immediate colour change from green to red due to the formation of the μ-hydroxo complex **P5** (Scheme 1).[12c] Such a transformation has also resulted in a large blue shift of the Soret band from 394 nm to 371 nm in dichloromethane.[12c]

Successful isolation of the oxidized complexes in a pure state has not been achieved by the electrochemical method owing to the presence of a large excess of supporting electrolytes. However, the $1e^-$- and $2e^-$- electron-oxidized products, **P3** and **P4**, are prepared by using one and two equivalents of iodine–silver perchlorate as oxidizing agents, respectively (see Experimental section in the ESI‡ for details), which are stable enough for their successful isolation in the solid state and one of them (**P3**) is also structurally characterized. Precipitated silver iodide is subsequently removed by centrifugation. Interestingly, neither iodine nor silver ions alone can oxidize **P2** under the conditions used here, as reported earlier.[15] The *in situ* generated $1e^-$- and $2e^-$- electron-oxidized products are identical to those prepared by the electrochemical oxidations and have also been confirmed by ESI-MS spectrometry. The spectrum of **P3** (in positive-ion mode) has revealed a peak at *m*/*z* 1216.5835, which has been assigned for $[\mathbf{P2}]^+$ (Fig. S2‡), and the spectrum of **P4** (in positive-ion mode) has shown a peak at *m*/*z* 608.2997, which is assigned for $[\mathbf{P2}]^{2+}$ (Fig. S3‡). The isotopic distribution patterns of the experimental mass have nicely correlated with calculated patterns, confirming the formation of the complexes. The oxidized complex **P3** exhibits characteristic stretching frequencies for the ClO_4^- group at 624 and 1108 cm^{-1} in the IR spectrum. The IR marker bands[16] for the porphyrin π-cation radical are also observed at 1554 cm^{-1} and 1629 cm^{-1}, characteristic of the asymmetric C_α–C_{meso} and C_β–C_β stretching modes, respectively, which are indeed absent in the unoxidized complex (Fig. S4‡).

To further elucidate the experimentally observed variations in the UV-vis-NIR spectrum, we conducted time-dependent

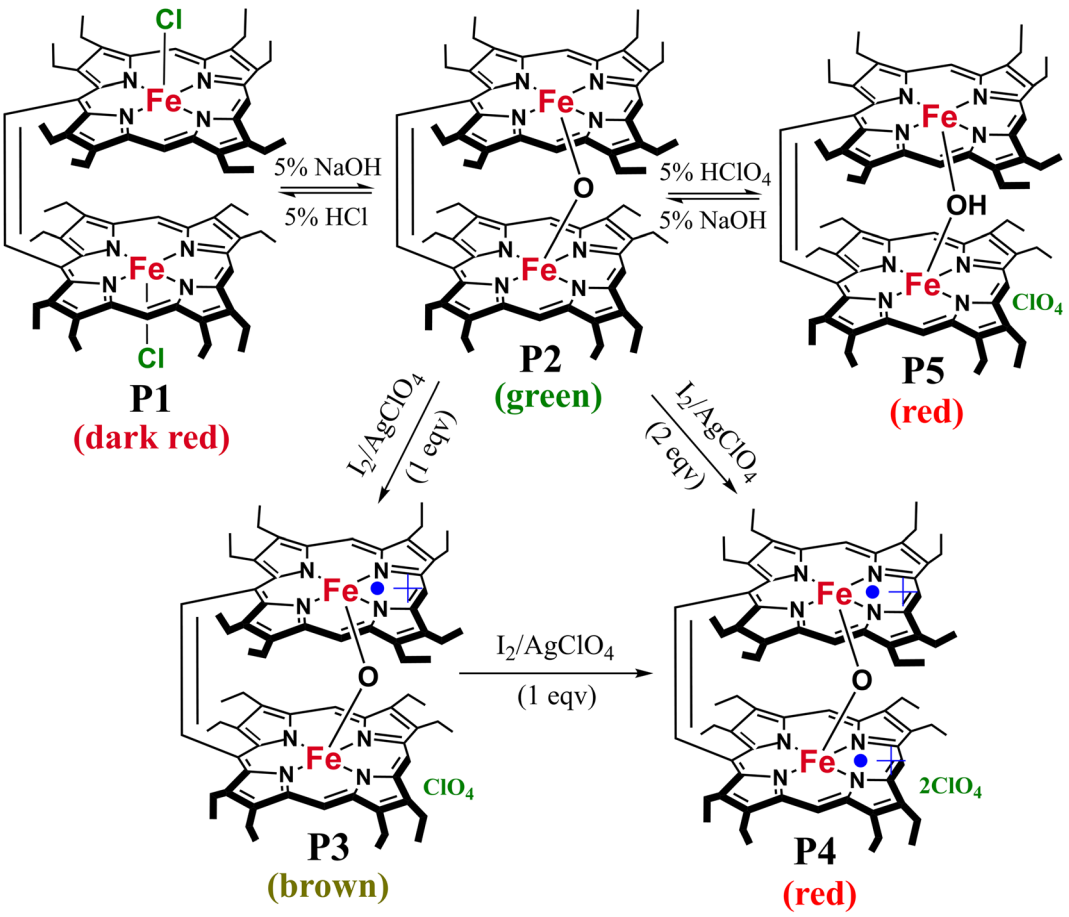

Scheme 1 Synthetic outline of the Fe(III) complexes and their abbreviations.

density functional theory (TD-DFT) calculations (see computational details in the ESI‡). The results from our theoretical calculations align well with the trends observed in the experimental data (Fig. 1C). Specifically, the TD-DFT analysis indicates a blue shift in the transition from **P2** to **P3**, where the Soret band shifts from 398 nm to 347 nm (Fig. S5 and S6‡). This observed blue shift in the Soret band from species **P2** to **P3**, followed by **P4**, was accurately replicated through TD-DFT calculations. The computed Soret bands at 398 nm, 347 nm, and 338 nm for species **P2**, **P3**, and **P4**, respectively, grossly match the experimental values of 394 nm, 383 nm, and 376 nm, respectively (Fig. S5–S7; see also Table S15‡ for excited state energies with corresponding oscillator strengths).

Crystallographic characterization of P3

Slow diffusion of *n*-hexane into a chloroform solution of the 1e$^-$-oxidized complex **P3** at room temperature produced dark brown crystals from which an appropriate crystal was chosen for X-ray diffraction experiments. The molecule crystallizes in the monoclinic crystal system with the *C*2/*c* space group (Table S1a‡). A perspective view of the molecule is shown in Fig. 2 and the selected bond distances and angles are given in Table S1b.‡

The two iron centres in the oxidized complex **P3** are in a five-coordinate square-pyramidal geometry and arranged in a cofacial manner. The average Fe–O and Fe–N_{por} bond lengths are 1.948(2) and 2.008(5) Å, respectively, whereas, for the unoxidized complex **P2**, the same distances are 1.783(3) and 2.085(3) Å.[13] As can be seen, the Fe–O and Fe–N_{por} distances significantly increase and decrease, respectively, upon 1e$^-$-oxidation. The iron atom is displaced by 0.41 Å from the least-square plane of the $C_{20}N_4$ porphyrinato core in **P3**, a distance that is significantly lower than that of 0.61 and 0.65 Å observed for cores I and II, respectively, in **P2**. The angle between the two least-square planes of the $C_{20}N_4$ porphyrinato core (Fig. S8‡) is decreased to 25.8° in **P3** from 27.7° in **P2**.

The close approach of the two porphyrin rings leads to a core deformation. The distortion of the porphyrin rings has increased in **P3** compared to that of unoxidized complex **P2** as can be seen in Fig. 3. The average displacement of atoms from the least-square plane of the $C_{20}N_4$ porphyrinato core (Δ_{24}) values are 0.14 and 0.23 Å for **P2** and **P3**, respectively. In contrast, both the rings are nearly planar in $[Fe(OEP)]_2O$.[17] The mean porphyrin plane separation (MPS) between the two rings is decreased on going from **P2** to **P3**, thereby enhancing the intermacrocyclic interactions. The *meso*-carbons that are connected through the bridging atoms are found to be displaced mostly. The Fe···Fe nonbonding distance has also been increased from 3.453 Å in **P2** to 3.694 Å in **P3**. The most unique feature of the structure of **P3** is the remarkably bent Fe–O–Fe unit with an angle of 143.0(3)° while the two macrocycles in the molecule are fully eclipsed geometrically. In contrast, the Fe–O–Fe unit is at 150.9(2)° in **P2**.

Table 1 compares the structural and geometrical features of **P2** with those of the corresponding unbridged $[Fe(OEP)]_2O$, **P3**, and the closely related μ-hydroxo complex **P5**. As observed, the

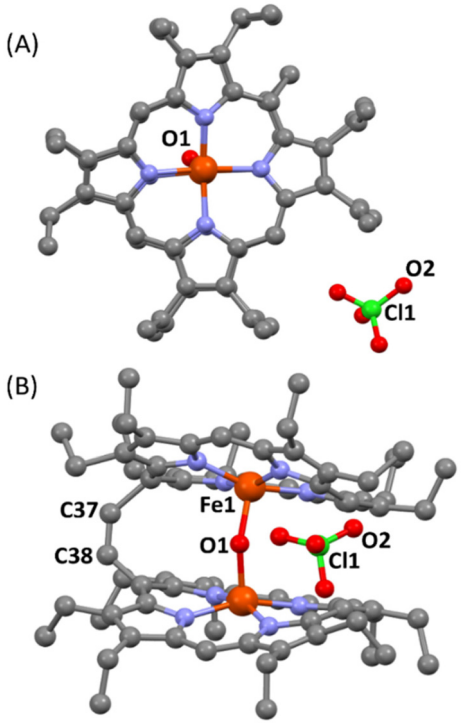

Fig. 2 (A) top view and (B) side view of the molecular structure of **P3** at 100 K. Hydrogen atoms have been omitted for clarity.

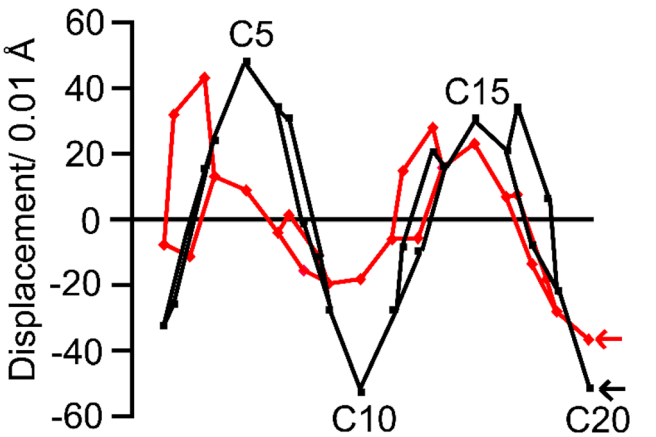

Fig. 3 Out-of-plane displacements (in units of 0.01 Å) of the porphyrin core atoms from the mean plane of the $C_{20}N_4$ porphyrin core for **P2** (red) and **P3** (black). The horizontal axis represents the atom number in the macrocycle showing the bond connectivity between atoms. Arrows show the positions of the bridged *meso*-carbons of the respective complexes.

Fe–O and Fe–N_{por} distances significantly increase and decrease, respectively, in going from **P2** to **P3**. In sharp contrast, the average Fe–N_{por} distances in **P5** are found to be 2.048(4) and 2.051(4) Å for the two porphyrin cores, which are substantially higher than that in **P3**. A hydrogen-bonding interaction is observed in **P5** between the μ-OH proton and oxygen

Table 1 Selected structural parameters for $[Fe(OEP)]_2O$, **P2**, **P3** and **P5**

		P2			**P5**	
	$[Fe(OEP)]_2O$ (monoclinic)	Core I	Core II	**P3**	Core I	Core II
Fe–O (Å)	1.755(10)	1.785(3),	1.781(3)	1.948(2)	1.937(4)	1.949(4)
Fe–N_{por} (Å)	2.080(5)	2.089(3)	2.081(4)	2.008(5)	2.048(4)	2.051(4)
Fe–O–Fe (°)	176.2(2)	150.9(2)		143.0(3)	143.85(2)	
Δ_{24}^{Fe} [a] (Å)	0.54	0.61	0.65	0.41	0.47	0.45
Fe···Fe (Å)	3.503(4)	3.453(1)		3.694	3.693(1)	
Interplanar angle[b] (°)	2.7	27.7		25.8	23.6	
MPS[c] (Å)	4.60	4.51		4.00	4.47	
Δ_{24}[d] (Å)	0.03	0.14		0.23	0.09	
Twist angle[e] (°)	16.8	0.6		1.2	5.82	
closest contact[f] (Å)	4.47	3.111(8)		3.483	2.871(8)	
Ref.	17	13		This work	12*c*	

[a] Displacement of iron from the least-square plane of the $C_{20}N_4$ porphyrinato core. [b] Angle between the two least-square planes (24 atoms). [c] Distance between the two least-square planes (24 atoms). [d] Average displacement of atoms from the least-square plane (24 atoms). [e] Average of the four N–Fe–Fe′–N′ dihedral angles. [f] Distance between two bridged *meso*-carbons.

atom of the water molecule (O1–O1 W, 2.756(10) Å).[12c] The iron atom is displaced by 0.41 Å from the least-square plane of the $C_{20}N_4$ porphyrinato core in **P3**. The value is somewhat higher in **P5** where the displacements of each iron(III) atom are 0.47 and 0.45 Å from the mean plane of the $C_{20}N_4$ porphyrinato core.[12c] The mean plane separation (MPS) between the two porphyrin rings is significantly narrower in **P3** and follows the order: $[Fe(OEP)]_2O$ > **P2** > **P5** > **P3**. Due to the close proximity of the two porphyrin rings, the cores are most distorted in **P3** as compared to **P2**, **P5**, and $[Fe(OEP)]_2O$.

The porphyrin rings are highly distorted in the $1e^-$-oxidized complex and can be visualized easily by looking at the out-of-plane displacement plots of the porphyrin core atoms as displayed in Fig. 3. Indeed, the distortion increases upon oxidation of just one of the rings enabling stronger inter-porphyrinic interactions through space due to the extreme closeness of the two porphyrin macrocycles (*vide supra*). Such distortions are also known to change various chemical and electrochemical properties of the molecule.[18–22]

EPR spectroscopy

Fig. S9‡ shows the EPR spectrum (in dichloromethane at 120 K) of **P3**. However, **P2** is EPR silent because of the strong antiferromagnetic coupling between the two Fe(III) central ions, whereas the one-electron-oxidized product **P3** shows a π-cation radical with its EPR spectrum centred at g = 1.99 (ΔH = 105 G). Moreover, the two-electron-oxidized species, **P4**, has also been found to be EPR silent due to the generation of dication di-radical species where there is a strong antiferromagnetic exchange interaction between the unpaired spins of Fe(III)–Fe(III) metal centres, Fe(III)–porphyrin π-cation radical and radical–radical interaction of the porphyrins.

^{1}H NMR spectroscopy

The structure and properties of the paramagnetic complexes in solution can be determined from ^{1}H NMR spectroscopy.[22–25] The oxidation of **P2** in $CDCl_3$ (after passing through basic alumina) at 295 K using iodine–silver perchlorate has been monitored by ^{1}H NMR spectroscopy. Fig. 4 shows the relevant spectra obtained from the reaction between **P2** and an acetonitrile solution of the oxidant *viz*. iodine–silver perchlorate. The data are presented so that the methylene and *meso*-resonances, which are expected to show large hyperfine shifts, are clearly visible. The methyl resonances in the diamagnetic region have been omitted to show a clear picture of the others.

The ^{1}H NMR spectrum of **P2** (shown in trace A) is relatively broad having four diastereotopic methylene protons at 4.9(2), 5.6, and 5.9 ppm along with two broad *meso*-resonances at 6.5 and 6.7 ppm in a 1 : 2 intensity ratio and the bridging –C*H* signal appears at 15.1 ppm. The presence of four methylene resonances in **P2** can be attributed to the fully eclipsed face-to-face orientation of the two rings generating an additional C_2 symmetry as is also observed in the X-ray structure of the complex.[13]

However, after the addition of 1.00 molar equivalent in total of iodine–silver perchlorate, the one-electron-oxidized product **P3** is produced, and the resultant ^{1}H NMR spectrum is shown in trace B. The eight diastereotopic methylene proton signals spread from 9 to 25 ppm and two *meso*-resonances appearing at 12.3 and 11.9 ppm in a 1 : 2 ratio also demonstrate the cofacial nature of the oxidized species **P3** in solution.

Small isotropic shifts in trace A are reflections of the weak paramagnetic nature resulting in strong antiferromagnetic coupling between two iron centres through the oxo bridge in **P2**. However, after $1e^-$-oxidation, both *meso*- and the methylene protons are downfield shifted and a well-resolved ^{1}H NMR spectrum (trace B) is obtained, which differs from that of the parent Fe(III) μ-oxo complex (trace A) most significantly in terms of larger isotropic shifts and the number of ethylene proton signals. The large isotropic shifts suggest porphyrin π-cation radical characteristics and also indicate relatively weaker antiferromagnetic coupling between the two iron centres as compared to **P2**.[11–13] Also, the ^{1}H NMR spectrum of

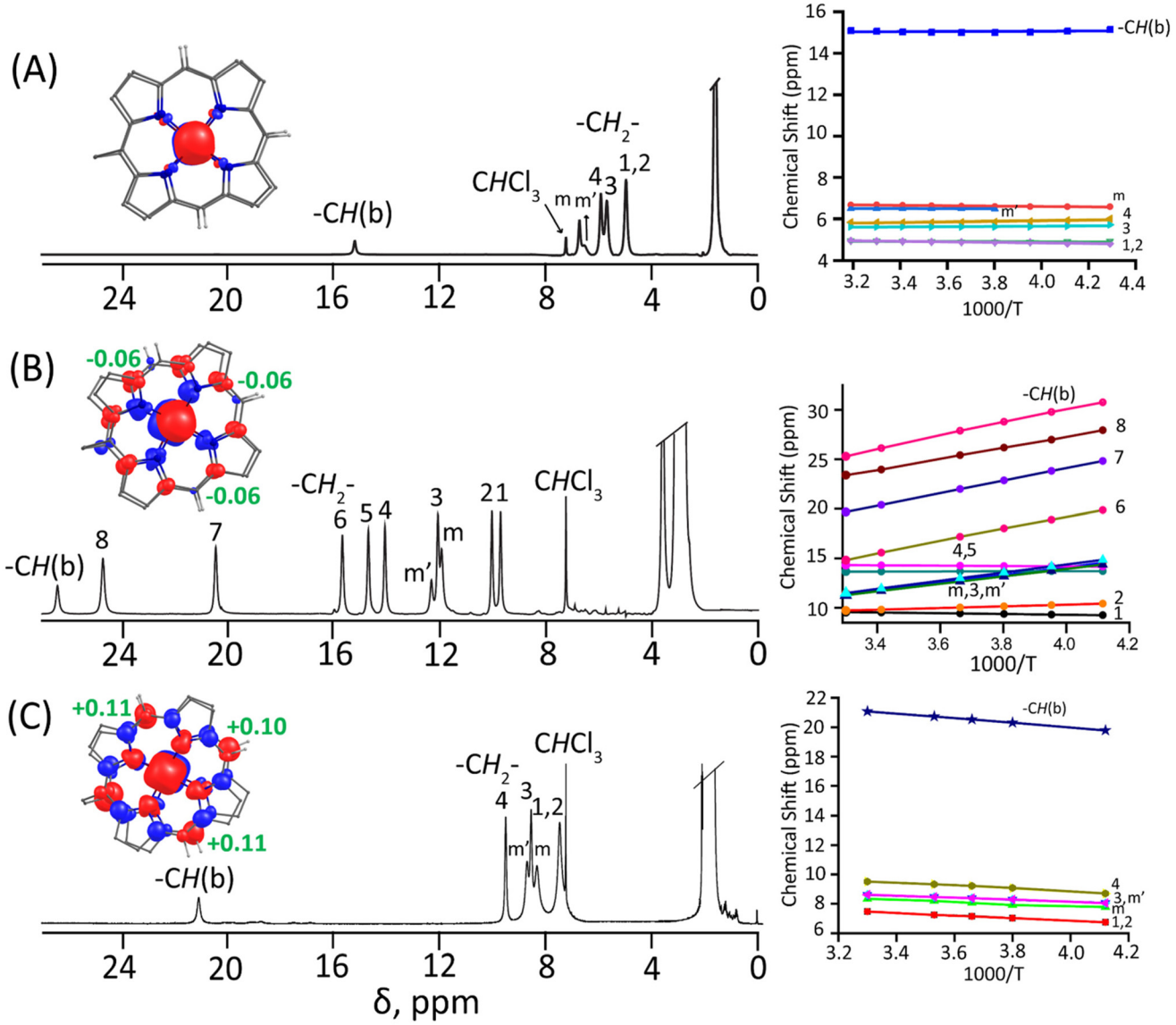

Fig. 4 ^{1}H NMR spectra (on the left) (in $CDCl_3$ at 295 K) and, Curie plots (on the right) of some of the proton signals of (A) **P2**, (B) **P3**, and (C) **P4**. The proton numbering scheme is shown in Fig. S8A.‡ The methylene CH_2 protons are numbered either as 1–8 or 1–4. The figure in each inset shows the corresponding spin density plots, where only *meso*-H atoms are shown and the rest of the H atoms are omitted for clarity. The red and blue isosurfaces show the positive and negative spin density plots.

P3 is distinctly different from that of the corresponding μ-hydroxo complex **P5** (Fig. 5). As can be seen, **P5** displays eight sharp methylene proton signals within the narrow range of δ = 16.9 ppm to 20.2 ppm, two *meso*-signals in a 2 : 1 intensity ratio at −3.9 and −12.4 ppm, and only one bridging –C*H* proton at 48.8 ppm.[12c] The addition of 2.0 molar equivalent of iodine–silver perchlorate in acetonitrile completely changed the ^{1}H NMR spectral pattern, again due to the formation of the two-electron-oxidized product **P4** and its spectrum is shown in trace C of Fig. 4. The four diastereotopic methylene proton signals of **P4** appear at 7.4, 8.5, and 9.5 ppm, and the bridging –C*H* signal comes at 21 ppm. Two broad *meso*-proton signals appear at 8.3 and 8.7 ppm. The ^{1}H NMR spectral pattern is indicative of very strong antiferromagnetic coupling between two iron centres.

Curie plots for some of the proton signals of **P2**, **P3**, and **P4** are shown in Fig. 4 and the linear relationship between the chemical shift and temperature suggests a single spin state of the Fe(III) centre over the experimental temperature range. Most interestingly, the nature of the Curie plots is distinctly different between **P3** and **P4** as they behave in opposite manners upon varying the temperature. For example, most of the signals (besides the two CH_2 protons of the ethyl substituents) of **P3** follow the Curie law while all the protons of **P4** display anti-Curie behavior. The Curie plot of **P2** suggests that there is no significant change in the chemical shift of the

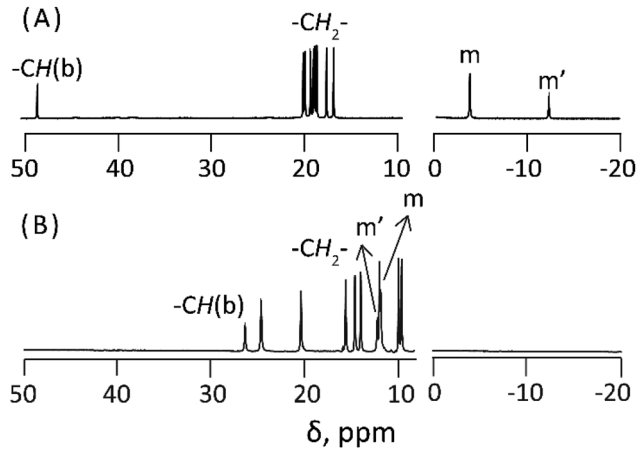

Fig. 5 ^{1}H NMR spectra (in $CDCl_3$ at 295 K) of (A) **P5** and (B) **P3**. The proton numbering scheme is shown in Fig. S8.‡

protons with respect to the change in temperature (Fig. 4A, right).

It would be important to compare here the ^{1}H NMR spectra between the μ-oxo dimer **P2** and its $2e^-$-oxidized complex **P4**, which are also shown in Fig. 4. The spectrum of **P2** in $CDCl_3$ displays the four diastereotopic methylene protons at 4.9(2), 5.6, and 5.9 ppm, two broad *meso*-resonances at 6.5 and 6.7 in 1 : 2 ratios while the bridging ethylene signal comes at 15.1 ppm. Such small isotropic shifts as observed in the ^{1}H NMR spectrum of μ-oxo complex **P2** reflect the weak paramagnetic characteristic as being a consequence of strong antiferromagnetic coupling through the oxo bridge, which has also been reflected in the small shifts of the signals over the temperature range.[13] On the other hand, complex **P4** displays four diastereotopic methylene proton signals at 7.4, 8.5, and 9.5 ppm while the bridging –C*H* signal comes at 21 ppm. Two broad *meso*-proton signals appear at 8.3 and 8.7 ppm in the oxidized complex. The ^{1}H NMR spectral pattern of **P4** also indicates very strong anti-ferromagnetic coupling between two iron(III) centres. However, the isotropic shifts that are observed in **P4** are larger than that of **P2** and thus indicative of slightly lower anti-ferromagnetic coupling in **P4**, which has also been observed in magnetic investigations in the solid state (*vide infra*). The shift in the *meso*-proton signals in **P2**, **P3**, and **P4** from ∼6 ppm to ∼12 ppm followed by ∼8 ppm, respectively, is also supported by the spin density plots (Fig. 4, inset). Negative spin densities are noted on *meso*-carbon atoms in **P3**, which results in downfield shifts of the *meso*-proton signals while positive spin densities are observed in **P4** resulting in upfield shifts of the *meso*-proton signals.

DFT calculations

To further shed light on the observed ^{1}H NMR spectra of **P2–P4**, we have performed ^{1}H NMR calculations using the ORCA suite (see computational details in the ESI‡).[26,27] DFT computation of ^{1}H NMR for **P2** (Table 2) suggests that the chemical shift for bridging ethene protons (CH═CH) is ∼9.0 ppm, which is underestimated with respect to the reported experimental value of ∼15.0 ppm. Similarly, the chemical shifts corresponding to methylene (CH_2) protons are computed as being in the range of 0.1–3.6 ppm, which is in close agreement with the experimental values of 4.9–5.9 ppm. Also, the average chemical shift for *meso*-protons m and m′ was computed as 9.5 ppm and 8.1 ppm, and this is also consistent with the experimentally reported values of 6.7 and 6.5 ppm, respectively (see Table S2‡). Similar to **P2**, in **P3** and **P4** the computed chemical shift for CH═CH protons was found to be underestimated; however, the pattern of the computed chemical shift (downfield on going from **P2** to **P3** followed by an upfield shift in **P4**) was found to be well reproduced in the computed data. The progression of chemical shift towards downfield values on going from **P2** to **P3** followed by the upfield shift in **P4** was attributed to the following reasons: (i) the ground spin states for **P2** and **P4** are singlet (total spin, S_T = 0) due to the strong magnetic exchange present between the spin centres (both are EPR silent) while **P3** is EPR active with S_T = 1/2 ground state, which results in strong hyperfine interaction of the ^{1}H proton in the S_T = 1/2 system leading to the downfield shift of the δ values; (ii) the J_{Fe-Fe} interaction is significantly weaker in **P3** compared to that in **P2** and **P4** (see Magnetic measurement section). The computed chemical shifts in **P3** and **P4** for methylene, m and m′ protons were found to be close to the experimentally observed values (see Tables S3 and S4‡). It is also interesting to note that the chemical shift of the protons in **P4** is downfield shifted compared to that of **P2**, though both have singlet ground states. This is due to the fact that the J_{Fe-Fe} in **P2** (-130 cm^{-1}) is stronger than that in the **P4** complex (-116 cm^{-1}), *vide infra*.

We found that for species **P3** and **P4**, the temperature dependence of proton chemical shift is just the opposite. While **P3** follows the Curie law, **P4** follows the anti-Curie law. To rationalise the above findings, we analysed the isotropic proton shift (IPS) that results due to the coupling between I (the nuclear magnetic quantum number) and S (the electron spin of the unpaired electron).[28] The IPS consists of the Fermi contact shift (CS) and the dipolar shift (DS), and it is given by

Table 2 The B3LYP-computed ^{1}H NMR chemical shift (in ppm) of complex **P2**. The figures in bold font in parentheses show the experimental values

P2	CH═CH (DFT)	CH_2 (DFT)	H (m) (DFT)	H (m′) (DFT)
	9.0 (**15.1**)	3.6 to 0.10 (**4.9**)	11.4 (**6.7**)	8.7 (**6.5**)
	9.0 (**15.1**)	(**4.9**)	11.4 (**6.7**)	7.6 (**6.5**)
		(**5.6**)	6.65 (**6.7**)	
		(**5.9**)	8.80 (**6.7**)	
Average	9.0 (**15.1**)	3.3 (**4.9**)	9.5 (**6.7**)	8.1 (**6.5**)

McConnell and Robertson[29] in the following expression for I = 1/2 and spin S:

$$(\Delta H/H)_{IPS} = (\Delta H/H)_{CS} + (\Delta H/H)_{DS} \quad (1)$$

Here,

$$(\Delta H/H)_{CS} = -\frac{g\beta S(S+1)}{(\gamma_N/2\pi)3kT}\sum_i A_i \quad (2)$$

$$(\Delta H/H)_{DS} = 28g^2\beta^2\frac{\langle 3\cos^2\theta - 1\rangle}{(3kT)^2 r^3}D\,(\text{for } S = 5/2) \quad (3)$$

The D here is the axial zero-field splitting of the ground state S, while A is the hyperfine coupling constant of the ground state. The terms r, θ come from the polar coordinates for individual protons. We have computed the hyperfine coupling constant for the bridging CH=CH proton, *meso*-proton (m/m′), and the ethylene protons for **P3** and **P4**, respectively, using *ab initio* CASSCF calculations on the optimised geometry employing established protocols as previously reported.[30] It is found that for CH=CH and m/m′/methylene protons, the average A for **P3** (S_T = 1/2) are ∼−1.68 MHz and 2.1/2.2/0.4 MHz, respectively (see Table S5‡), while for the ground state (S_T = 0) of **P4** it is 0. Similarly, the 1st (S_T = 3/2) and 2nd (S_T = 5/2) excited states of **P3** show A values for the CH=CH/m/m′/methylene protons of ∼−1.0/0.3/1.6/1.4 MHz and ∼−0.4/0.04/0.5/0.6 MHz, respectively (see Tables S6 and S7‡). For **P4**, the 1st (S_T = 1) and 2nd (S_T = 2) excited states exhibit A values for CH=CH/m/m′/methylene protons of ∼2.5/0.9/−3.8/−1.1 MHz and ∼0.2/0.3/−0.1/−0.1 MHz, respectively (see Tables S8 and S9‡). The axial ZFS parameter D value for each Fe metal centre in **P3** and **P4** was computed using *ab initio* CASSCF/NEVPT2 calculations following the established protocols.[31] The computed D values were found to be ∼+3.0 cm^{-1} and +1.0 cm^{-1}, respectively, with estimated E/D of 0.007 and 0.002 (see Table S10‡).[32] Eqn (2) and (3) suggest that the CS contribution follows a $\propto 1/T$ relationship, while the DS contribution has a $\propto 1/T^2$ relationship, and the parameters g, β, k and γ_N are constants.

From Fig. S10(C and D),‡ it is clear that on decreasing the temperature from 300 K (1000/T = 3.3 K^{-1}) to 235 K (1000/T = 4.2 K^{-1}), the population of the ground state, S_T = 1/2, for **P3** increases from 45% to 50% while for excited states the percentage population decreases. Therefore, $\sum Ai$ and $\sum Ai/T$ are expected to increase on decreasing the temperature followed by an increase in the value of $(\Delta H/H)_{CS}$. Similarly, the D/T^2 value will also increase on decreasing the temperature followed by an increase in the value of $(\Delta H/H)_{DS}$. Therefore, the overall $(\Delta H/H)_{IPS}$ is expected to increase on decreasing the temperature (1000/T = 3.3 K^{-1} → 1000/T = 4.2 K^{-1}). Hence, due to the increase in the isotropic proton shift, the overall chemical shift of almost all protons increases by decreasing the temperature (see Fig. 4B) in the case of **P3**.

On the other hand, Fig. S10(E and F)‡ suggests that the percentage of the Boltzmann population of the diamagnetic ground state (S_T = 0) of **P4** increases by decreasing the temperature from 300 K to 235 K and the % population for excited states becomes nearly zero. Therefore, ongoing from 1000/T = 3.3 K^{-1} → 1000/T = 4.2 K^{-1}, the $\sum Ai/T$ value is expected to decrease significantly, and D/T^2 will increase, albeit with the former dominating the overall contribution. Therefore, overall, a slight decrease in the $(\Delta H/H)_{IPS}$ is noted, and hence the overall chemical shift decreases for all the protons in the case of **P4** on decreasing the temperature (1000/T = 3.3 K^{-1} → 1000/T = 4.2 K^{-1}). Therefore, in **P3**, as the temperature decreases, the ground spin state (S = 1/2) population is expected to increase, resulting in an enhancement of hyperfine coupling (note the A values for this state are larger than those of the first excited state). This leads to a downfield shift of the ^{1}H. In contrast, in **P4**, the ground state (S = 0) is diamagnetic, while the excited state (S = 1) is paramagnetic. As the temperature decreases, the population of the diamagnetic ground state (S = 0) increases, while the population of the paramagnetic excited state (S = 1), which contributes to hyperfine coupling, decreases. Consequently, an upfield shift of the ^{1}H proton is observed in **P4** with decreasing temperature. The detailed examination of the Curie plot for neutral complex **P2** indicates that the temperature-dependent change in the chemical shift (Fig. 4A, right) is negligible. This is attributed to the fact that the excited states, which are over 3–40 kJ mol^{-1} higher in energy, are completely depopulated as available thermal energy in the 300 K–235 K temperature range is 1.9 kJ mol^{-1}–2.5 kJ mol^{-1}. Consequently, the ground singlet state remains predominantly populated (Fig. S10A and B‡). As a result, varying the temperature from 300 K to 235 K does not significantly alter the Boltzmann population of the ground state, leading to an insignificant variation in the chemical shift.

Magnetic measurements

Variable temperature magnetic susceptibility measurements for crystalline samples **P2**, **P3**, and **P4** have been carried out between 5 and 300 K using an applied magnetic field of 0.1 T. Temperature-dependent magnetization plots for the complexes are shown in Fig. 6. The $\chi_M T$ values for **P2**, **P3**, and **P4** at room temperature are found to be ∼0.9 cm^3 K mol^{-1}, 3.0 cm^3 K mol^{-1}, and 1.3 cm^3 K mol^{-1}, respectively, and these values differ significantly from the theoretical values of 8.75, 9.125 and 9.5 cm^3 K mol^{-1}, which are expected based on uncoupled (two high-spin Fe(III) for **P2**, two high-spin Fe(III) and one radical for **P3**, and two high-spin Fe(III) and two radicals for **P4**) systems. This suggests the presence of strong antiferromagnetic coupling that persists even at room temperature. As the temperature decreases, the $\chi_M T$ decreases gradually until 50 K and then decreases sharply, suggesting various competing exchanges and zero-field splitting (ZFS) that are operational in these complexes. One magnetic exchange (J_{Fe-Fe}) in **P2**, two magnetic exchanges (J_{Fe-Fe} and J_{Fe-r}) in **P3**, and three magnetic exchanges in (J_{Fe-Fe}, J_{Fe-r}, and J_{r-r}) in **P4** are possible

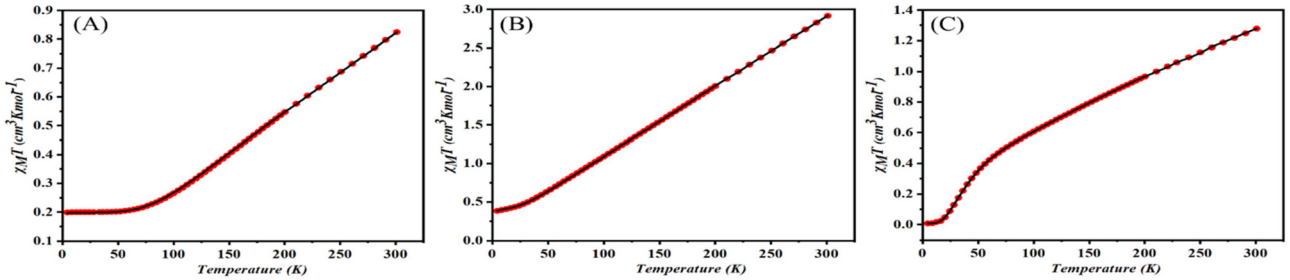

Fig. 6 Plots of DC magnetic susceptibility, $\chi_M T$ *vs.* *T*, for (A) **P2**, (B) **P3** and (C) **P4** (red dotted lines). The solid black lines represent the simulation from the PHI suite.[41]

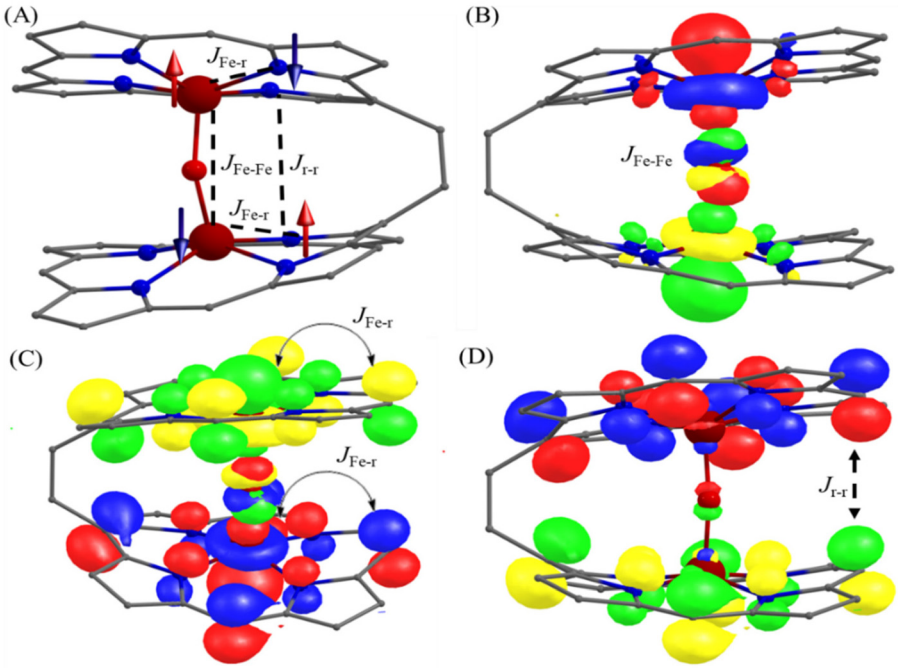

Fig. 7 (A) Several possible magnetic exchanges (*J* values) present in **P4**. (B) Schematic diagram showing the orbital overlap between d_{z^2}–p_z–d_{z^2} for J_{Fe-Fe}. (C) and (D) Representative orbital overlap diagrams for J_{Fe-r} (HOMO of porphyrin and Fe d_{z^2}) and J_{r-r} (HOMO of both the porphyrins), respectively. The isosurface of one porphyrin moiety is shown by red (+) and blue (–) while for the other porphyrin moiety the isosurface is indicated by green (+) and yellow (–) colours. The isosurface value of 0.05 au was used.

(see Fig. 7A). The following exchange Hamiltonians have been used to compute the several values of *J*:

$$\hat{H} = -2J_{\mathrm{Fe-Fe}}S_{\mathrm{Fe1}}S_{\mathrm{Fe2}} \text{ (for } \mathbf{P2})$$

$$\hat{H} = -2\left[J_{\mathrm{Fe-Fe}}S_{\mathrm{Fe1}}S_{\mathrm{Fe2}} + J_{Fe-\mathrm{r}}S_{\mathrm{Fe1}}S_{\mathrm{Fe}^1_{\mathrm{rad}}}\right] \text{ (for } \mathbf{P3})$$

$$\hat{H} = -2[J_{\mathrm{Fe-Fe}}S_{\mathrm{Fe1}}S_{\mathrm{Fe2}} + J_{\mathrm{Fe-r}}\left(S_{\mathrm{Fe1}}S_{\mathrm{Fe}^1_{\mathrm{rad}}} + S_{\mathrm{Fe2}}S_{\mathrm{Fe}^2_{\mathrm{rad}}}\right) + J_{\mathrm{r-r}}S_{\mathrm{Fe}^1_{\mathrm{rad}}}S_{\mathrm{Fe}^2_{\mathrm{rad}}} \text{ (for } \mathbf{P4})$$

As fitting the magnetic susceptibility with different exchanges, particularly in complex **P4**, can lead to an over-parameterization problem (see Fig. S17 and Table S14‡), we have performed broken symmetry density functional theory[33] (BS-DFT) calculations in the Gaussian 16 suite[34] using the unrestricted B3LYP functional,[35] def2TZVP basis set[36] for Fe and def2SVP basis set for other atoms (see computational details in the ESI‡ for more information), which has a proven track record of yielding good numerical estimates of *J* values.[37–39] The DFT-optimized geometries are well corroborated with the experimental X-ray structures (see Fig. S11–S13‡). The J_{Fe-Fe} interaction describes the magnetic exchange between both the Fe(III) (S = 5/2) centres, J_{Fe-r} represents the interaction between the Fe(III) (S = 5/2) and the porphyrin π-cation radical (S = 1/2), while J_{r-r} shows the interaction

Table 3 Experimentally simulated and DFT-computed exchange-coupling constants (J values) in **P2**, **P3** and **P4**

		P2			**P3**			**P4**		
Exchange type	Spin centres	J_{DFT} (cm^{-1})	J_{sim}, (DFT guided) (cm^{-1})	J_{sim}, (DFT unguided) (cm^{-1})	J_{DFT} (cm^{-1})	J_{sim}, (DFT guided) (cm^{-1})	J_{sim}, (DFT unguided) (cm^{-1})	J_{DFT} (cm^{-1})	J_{sim}, (DFT guided) (cm^{-1})	J_{sim}, (DFT unguided) (cm^{-1})
J_{Fe-Fe}	Fe1–Fe2	−113.4	−130.4	−130.4	−51.9	−37.8	−41.5	−106.1	−116.1	−179.2
J_{Fe-r}	$Fe1–Fe1_{rad}$	—	—	—	−14.0	−16.5	0.9	−26.5	−27.2	24.6
J_{r-r}	$Fe1_{rad}–Fe2_{rad}$	—	—	—	—	—	—	−3.1	−2.4	−3.4

between both the porphyrin π-cation radicals (S = 1/2) (see Fig. 7B–D). The BS–DFT calculations of complex **P2** estimate the J_{Fe-Fe} value of −113.4 cm^{-1} suggesting a strong antiferromagnetic exchange between the Fe(III) centres (see Table 3). The computed J_{Fe-Fe} is modified to −106 cm^{-1} and 102 cm^{-1} in the presence of chloroform and dichloromethane solvent, respectively, which suggests a very minimal effect of solvent on magnetic exchange. Magneto-structural correlation established already by Boča and coworkers[40] suggests that the interaction is strongly correlated with the Fe–O–Fe angle and Fe–O distance. Here, the X-ray (DFT computed) Fe–O distance and Fe–O–Fe angles for **P2** are 1.785/1.781 (1.770/1.773) Å and 150.9° (155.1°), respectively (see Table 1 for X-ray and Fig. 8A for DFT-computed geometrical parameters), and for these structural parameters the expected exchange interaction is ∼−120 cm^{-1}, and the DFT-computed J_{Fe-Fe} as well as the observed exchange from the PHI simulation is in close agreement with this estimate, offering confidence in the estimated J value. The strong antiferromagnetic exchange between the Fe(III) centres is due to the very strong overlap between the d-orbitals of the Fe(III) centres through bridging $–O^{2-}–$ $p_x/p_y/p_z$ orbitals (see Table S11‡).

The super-exchange between the Fe(III) centres is also possible through the bridging –CH=CH– group. To understand various bridging group contributions to the net exchange interactions, we have constructed several model complexes where either the $–O^{2-}–$ bridging atom (J_O) or the –CH=CH– group ($J_{CH=CH}$) is kept and the other is removed/replaced by point charges (see computational details for the methodology employed and models used, Fig. S16‡). The values of J_O (exchange through the oxo bridge) and $J_{CH=CH}$ (exchange through the ethene bridge) are computed to be −117.0 cm^{-1} and +43.4 cm^{-1}, respectively. The above finding suggests that the antiferromagnetic exchange is triggered *via* the $–O^{2-}–$ bridging atom, while in its absence, the –CH=CH– group is expected to promote ferromagnetic coupling. This also suggests that when both groups are present simultaneously, there is a cooperative enhancement in antiferromagnetic coupling to the tune of −39.8 cm^{-1} (see the ESI‡ for details). The spin density plot of the BS and HS states of **P2** suggests that there is a significant spin density delocalization from both the Fe(III) centres to the bridging $–O^{2-}–$ as well as to the porphyrin rings (see Fig. 8A and S15‡). Similar complexes like ethane-bridged bis-Fe(III)-μ-oxo porphyrin dimer and diethylpyrrole-bridged bis-Fe(III)-μ-oxo porphyrin dimer also show strong antiferromagnetic coupling between two Fe^{III} centres having J_{Fe-Fe} values of −126.6 cm^{-1} and −137.7 cm^{-1}, respectively.[12b]

For **P3**, the DFT-computed J_{Fe-Fe} and J_{Fe-r} values were found to be −51.9 cm^{-1} and −14.0 cm^{-1}, respectively. A significantly low value of −51.9 cm^{-1} is because, upon $1e^-$-oxidation of **P2**, the Fe–O bond length (X-ray) increases from 1.78 Å (**P2**) to 1.94 Å (**P3**). Also, the Fe–O–Fe bond angle decreases from 150.9° (**P2**) to 143.0° (**P3**, see Table 1). Hence, the significant increase in Fe–O bond length and a moderate decrease in Fe–O–Fe bond angle causes a decrease in the J_{Fe-Fe} value as reported in the earlier magneto-structural correlations.[40] This observation is also supported by the computed overlap integral between the d-orbitals of both Fe(III) centres (see Tables S11 and S12‡). The orbital overlap figures also suggest that there is a very weak d_{z^2}(Fe)–$p_x/p_y/p_z(O^{2-})$–d_{z^2}(Fe) overlap in **P3** compared to **P2**, causing a significant decrease in the J_{Fe-Fe} value

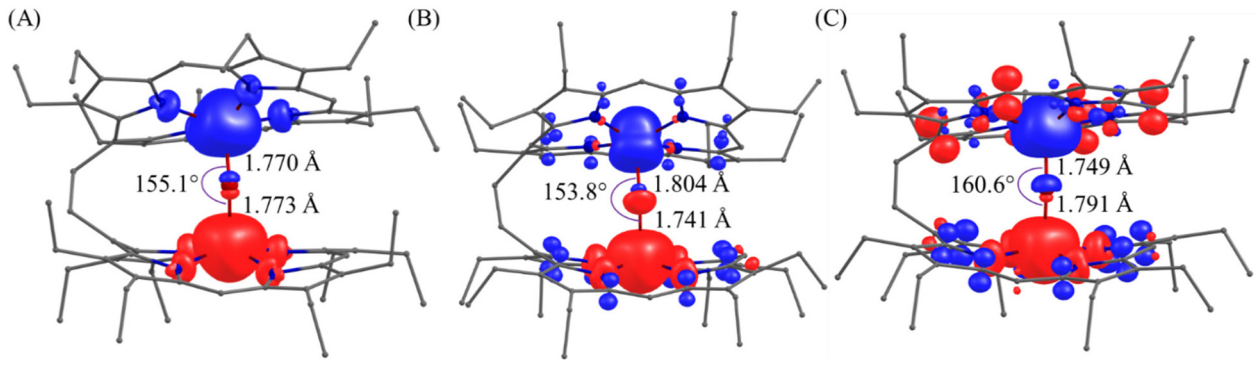

Fig. 8 Ground state spin-density plot of the DFT-optimized structures of (A) **P2** (singlet state), (B) **P3** (doublet state), and (C) **P4** (singlet state). Here, the bond lengths and angles shown are DFT-computed.

(see Fig. S14‡). Similar results were witnessed in the earlier report of the *cis*-ethene-bridged bis-Fe(III)-μ-hydroxo porphyrin dimer with ClO_4^- as the counter anion (*cis*-[Fe(OEP)]$_2$OH·ClO_4), where J_{Fe-Fe} = −34.0 cm^{-1} was noted and affirmed confidence in our chosen methodology.[12c]

For **P4**, one more interaction was considered, which is the coupling between two porphyrin π-cation radical spins (J_{r-r}). In this case, the DFT calculations yielded J_{Fe-Fe} = −106.1 cm^{-1}, J_{Fe-r} = −26.5 cm^{-1}, and J_{r-r} = −3.1 cm^{-1}. From the parameters obtained, it is evident that the extent of antiferromagnetic coupling between two Fe(III) centres, *i.e.*, J_{Fe-Fe}, decreased in going from **P2** to **P3** followed by an increase in **P4**. This is due to the fact that the Fe–O bond length increases from **P2** (1.78 Å) to **P3** (1.94 Å) followed by a decrease in **P4** (1.74 Å; see Fig. S11–S13‡). Similarly, the Fe–O–Fe bond angle also decreases going from **P2** (150.9°) to **P3** (143.0°) followed by an increase in **P4** (160.6°). The computed *J* values in **P4** are also supported by the significant overlap integral between the d-orbitals of Fe metal centres (see Table S13‡).

From the molecular structures of these three μ-oxo complexes, it is seen that the Fe–O–Fe angle follows the order: diethylpyrrole-bridged bis-Fe(III)-μ-oxo porphyrin dimer (151.9°) > **P2** (150.9°) > ethane-bridged bis-Fe(III)-μ-oxo porphyrin dimer (147.9°). The J_{Fe-Fe} value is dependent upon this Fe–O–Fe angle. The greater the value of this angle, the larger the extent of antiferromagnetic coupling between two Fe(III) centres. The significant spin delocalization from metal to ligand was also noted in complexes **P3** and **P4**, giving ground state spin density, S_T = 1/2 (**P3**) and S_T = 0 (**P4**), respectively (see Fig. 8B and C).

The computed *J* values from the DFT calculations were chosen as an initial estimate in order to perform the χT *vs.* *T* simulations using the program PHI.[41] The simulated plot matches well with the experimental χT *vs.* *T* plot (see Fig. 6), while the *J* values obtained from the simulation are also in close agreement with the DFT-computed magnetic exchange values (see Table 3). When we fit the χT *vs.* *T* plot without the guidance from the DFT-computed *J* values, it also matches equally well with the experimental plot (Fig. S17‡), but the obtained fits are not often unique and can give unreliable *J* values if the number of parameters employed is larger as in the case of **P3**/**P4**. These findings reiterate an established point that one should attempt to fit the magnetic data with DFT calculations when there are multiple exchange couplings possible.[42] Complexes **P2** and **P4** were found to be EPR silent due to the presence of strong magnetic exchange between the paramagnetic centres, which give an overall S_T = 0, while the excited state in **P2** (*S* = 5) and **P4** (*S* = 1) lie more than 40 kJ mol^{-1} and 8 kJ mol^{-1}, respectively, higher in energy (see Table S16‡ for spin ladders energies).

Conclusions

In the present work, a bis-Fe(III)-μ-oxo-porphyrin dimer **P2** where the two porphyrin units are covalently bridged by a rigid ethene linker has been utilized to study spin coupling upon stepwise oxidations. The complex contains a remarkably bent Fe–O–Fe unit bringing the two porphyrin macrocycles into close proximity, which results in strong intermacrocyclic interactions between them. As a result, the two cores become highly distorted and more electron-rich making the system readily oxidizable with four one-electron oxidations within the potential window of dichloromethane. After the addition of 1 molar equivalent in total of the oxidant (iodine–silver perchlorate), a well-resolved ^{1}H NMR spectrum is generated where the methylene protons are shifted downfield with respect to that of the parent complex **P2**. The porphyrin π-cation radical character of singly oxidized species **P3** is indicated by this large isotropic shift in the ^{1}H NMR signals. Upon 2e$^-$-oxidation, the nature of the NMR spectra is further changed, where the upfield shift of the methylene protons is again observed suggesting strong antiferromagnetic coupling between two Fe centres in **P4**. Interestingly, most of the proton signals in **P3** and **P4** behave differently upon varying the temperature and follow Curie and anti-Curie behaviour, respectively. Extensive DFT calculations coupled with *ab initio* CASSCF calculations on the ground and the excited states of these species rationalize the observation of the Curie *vs.* anti-Curie behaviour observed. In particular, the Curie plot observed for **P3** was found to correlate well with the *S* = 1/2 ground state resulting in large hyperfine coupling with ^{1}H nuclei. For complexes **P2** and **P4**, the variation observed was correlated to the strength of the magnetic coupling.

X-ray structure analysis of the 1e$^-$-oxidized complex revealed a remarkable bent Fe–O–Fe unit with a significant decrease and increase of the Fe–N_{por} and Fe–O distances, respectively, compared with the unoxidized complex. Thus, 1e$^-$-oxidation brings the two porphyrin macrocycles even closer to each other, which causes the porphyrin cores to become more distorted due to stronger intermacrocyclic interaction between them. Variable temperature magnetic susceptibility measurement of the polycrystalline samples **P2**, **P3** and **P4** showed that the extent of antiferromagnetic coupling between the two Fe(III) centres varies upon oxidation. **P2** shows very strong antiferromagnetic coupling with J_{Fe-Fe} = −130.4 cm^{-1}. After 1e$^-$-oxidation, this coupling is largely weakened giving the value of −37.8 cm^{-1}, which is also in accordance with the decrease in the Fe–O–Fe angle and increase in the Fe–O bond length in **P3** with respect to **P2**. The antiferromagnetic coupling again becomes stronger in **P4** with J_{Fe-Fe} = −116.1 cm^{-1}. DFT calculations suggest that both the Fe–O–Fe bond angle and the Fe–O bond distances play critical roles in determining the strength of *J* and all the computed results are consistent with experimental findings.

Author contributions

S.P.R. conceptualized and supervised the work and wrote the paper along with all other coworkers. S.B. and P.C. performed the experiments. R.K.T. and G.R. completed the magnetic

simulations and DFT calculations. All authors have analysed the results together.

Data availability

A comprehensive description of the synthesis and experimental procedures, including full characterisation data, details of instrumentation, and computational methods, can be found in the ESI.‡

CCDC 2377591 contains the supplementary crystallographic data for this paper.

Conflicts of interest

There are no conflicts to declare.

Acknowledgements

We would like to thank the Science and Engineering Research Board (SERB), India, SERB-STAR and and Council of Scientific and Industrial Research (CSIR), New Delhi for financial support. SPR thanks SERB for giving him the Science and Technology Award for Research (SERB-STAR). GR thanks SERB (SB/SJF/2019-20/12; CRG/2022/001697) for funding. SB, RKT and PC would like to thank DST-INSPIRE, CSIR, and IIT Kanpur, respectively, for their fellowships. The authors also thank Dr. Sudip Kumar Ghosh, Dr. Debangsu Sil, Dr. Firoz S. T. Khan and Dr. Sabyasachi Sarkar for their contributions at the initial stage of the project.

References

1 (*a*) W. Wang, A. D. Liang and S. J. Lippard, Coupling oxygen consumption with hydrocarbon oxidation in bacterial multicomponent monooxygenases, *Acc. Chem. Res.*, 2015, **48**, 2632; (*b*) S. Hematian, I. Garcia-Bosch and K. D. Karlin, Synthetic heme/copper assemblies: Toward an understanding of cytochrome *c* oxidase interactions with dioxygen and nitrogen oxides, *Acc. Chem. Res.*, 2015, **48**, 2462; (*c*) S. P. de Visser, J.-U. Rohde, Y.-M. Lee, J. Cho and W. Nam, Intrinsic properties and reactivities of mononuclear nonheme iron–oxygen complexes bearing the tetramethylcyclam ligand, *Coord. Chem. Rev.*, 2013, **257**, 381; (*d*) A. J. Jasniewski and L. Que Jr., Dioxygen activation by nonheme diiron enzymes: Diverse dioxygen adducts, high-valent intermediates and related model complexes, *Chem. Rev.*, 2018, **118**, 2554; (*e*) B. Battistella and K. Ray, O_2 and H_2O_2 activations at dinuclear Mn and Fe active sites, *Coord. Chem. Rev.*, 2020, **408**, 213176.

2 (*a*) D. M. Kurtz Jr., Oxo- and hydroxo-bridged diiron complexes: A chemical perspective on a biological unit, *Chem. Rev.*, 1990, **90**, 585; (*b*) J. B. Vincent, G. L. Olivier-Lilley and B. A. Averill, Proteins containing oxo-bridged dinuclear iron centers: A bioinorganic perspevtive, *Chem. Rev.*, 1990, **90**, 1447; (*c*) M. Fontecave, S. Ménage and C. Duboc-Toia, Functional models of non-heme diiron enzymes, *Coord. Chem. Rev.*, 1998, **178–180**, 1555; (*d*) E. I. Solomon, T. C. Brunold, M. I. Davis, J. N. Kemsley, S.-K. Lee, N. Lehnert, F. Neese, A. J. Skulan, Y.-S. Yang and J. Zhou, Geometric and Electronic Structure/Function Correlations in Non-Heme Iron Enzymes, *Chem. Rev.*, 2000, **100**, 235; (*e*) A. Trehoux, J.-P. Mahy and F. Avenier, A growing family of O_2 activating dinuclear iron enzymes with key catalytic diiron(III)-peroxo intermediates: Biological systems and chemical models, *Coord. Chem. Rev.*, 2016, **322**, 142.

3 (*a*) C. E. Tinberg and S. J. Lippard, Dioxygen activation in soluble methane monooxygenase, *Acc. Chem. Res.*, 2011, **44**, 280; (*b*) R. E. Stenkamp, Dioxygen and hemerythrin, *Chem. Rev.*, 1994, **94**, 715.

4 (*a*) N. Mitić, S. J. Smith, A. Neves, L. W. Guddat, L. R. Gahan and G. Schenk, The catalytic mechanisms of binuclear metallohydrolases, *Chem. Rev.*, 2006, **106**, 3338; (*b*) G. Schenk, N. Mitić, G. R. Hanson and P. Comba, Purple acid phosphatase: A journey into the function and mechanism of a colorful enzyme, *Coord. Chem. Rev.*, 2013, **257**, 473.

5 (*a*) M. Fontecave, S. Ménage and C. Duboc-Toia, Functional models of non-heme diiron enzymes, *Coord. Chem. Rev.*, 1998, **178–180**, 1555; (*b*) B. J. Wallar and J. D. Lipscomb, Dioxygen activation by enzymes containing binuclear non-heme iron clusters, *Chem. Rev.*, 1996, **96**, 2625.

6 (*a*) D. Sil, F. S. T. Khan and S. P. Rath, Effect of intermacrocyclic interactions: modulation of metal spin state in oxo/hydroxo/fluoro bridged diiron(III)/dimanganese(III) porphyrin dimers, *Adv. Inorg. Chem.*, 2023, **81**, 95; (*b*) A. B. Sorokin, Recent progress on exploring μ-oxo bridged binuclear porphyrinoid complexes in catalysis and material science, *Coord. Chem. Rev.*, 2019, **389**, 141; (*c*) T. Guchhait, S. Sasmal, F. S. T. Khan and S. P. Rath, Oxo- and hydroxo-bridged diiron (III) porphyrin dimers: Inorganic and bio-inorganic perspevtives and effects of intermacrocyclic interactions, *Coord. Chem. Rev.*, 2017, **337**, 112.

7 (*a*) V. Valderrey, G. Aragay and P. Ballester, Porphyrin tweezer receptors: Binding studies, conformational properties and applications, *Coord. Chem. Rev.*, 2014, **258–259**, 137; (*b*) I. Beletskaya, V. S. Tyurin, A. Y. Tsivadze, R. Guilard and C. Stern, Supramolecular chemistry of metalloporphyrins, *Chem. Rev.*, 2009, **109**, 1659; (*c*) J. Rosenthal and D. G. Nocera, Oxygen activation chemistry of Pacman and Hangman porphyrin architectures based on xanthene and dibenzofuran spacers, *Prog. Inorg. Chem.*, 2007, **55**, 483.

8 (*a*) J. P. Collman, P. S. Wagenknecht and J. E. Hutchison, Molecular catalysts for multielectron redox reactions of small molecules: The "cofacial metallodiporphyrin" approch, *Angew. Chem., Int. Ed. Engl.*, 1994, **33**, 1537; (*b*) M. O. Senge, K. R. Gerzevske, M. G. H. Vicente, T. P. Forsyth and K. M. Smith, Models for the photosynthetic reaction center- Synthesis and structure of porphyrin dimers with *cis*-, and *trans*-ethene and skewed hydroxymethylene bridges, *Angew. Chem., Int. Ed. Engl.*, 1993, **32**,

750; (*c*) P. Lang and M. Schwalbe, Pacman compounds: From energy transfer to cooperative catalysis, *Chem. – Eur. J.*, 2017, **23**, 17398.

9 (*a*) P. P. Roy, S. Kundu, J. Valdiviezo, G. Bullard, J. T. Fletcher, R. Liu, S.-J. Yang, P. Zhang, D. N. Beratan, M. J. Therien, N. Makri and G. R. Fleming, Synthetic Control of Exciton Dynamics in Bioinspired Cofacial Porphyrin Dimers, *J. Am. Chem. Soc.*, 2022, **144**, 6298; (*b*) A. Takai, C. P. Gros, J.-M. Barbe, R. Guilard and S. Fukuzumi, Enhanced Electron-Transfer Properties of Cofacial Porphyrin Dimers through p–p Interactions, *Chem. – Eur. J.*, 2009, **15**, 3110; (*c*) S. Faure, C. Stern, E. Espinosa, J. Douville, R. Guilard and P. D. Harvey, Triplet–Triplet Energy Transfer Controlled by the Donor–Acceptor Distance in Rigidly Held Palladium-Containing Cofacial Bisporphyrins, *Chem. – Eur. J.*, 2005, **11**, 3469; (*d*) J. T. Fletcher and M. J. Therien, Extreme Electronic Modulation of the Cofacial Porphyrin Structural Motif, *J. Am. Chem. Soc.*, 2002, **124**, 4298.

10 (*a*) Y. Kuramochi, M. Hashimoto and A. Satake, Methane formation induced *via* face-to-face orientation of cyclic Fe porphyrin dimer in photocatalytic CO_2 reduction, *Molecules*, 2024, **29**, 2453; (*b*) D. Zhang, M. R. Crawley, A. N. Oldacre, L. J. Kyle, S. N. MacMillan and T. R. Cook, Lowering the Symmetry of Cofacial Porphyrin Prisms for Selective Oxygen Reduction Electrocatalysis, *Inorg. Chem.*, 2023, **62**, 1766; (*c*) E. A. Mohamed, Z. N. Zahran and Y. Naruta, A flexible cofacial Fe porphyrin dimer as an extremely efficient and selective electrocatalyst for the CO_2 to CO conversion in non-aqueous and aqueous media, *J. Mater. Chem. A*, 2021, **9**, 18213; (*d*) D. Boskovic, S. Balakrishnan, S. Huang and G. F. Swiegers, Kinematic molecular manufacturing machines, *Coord. Chem. Rev.*, 2016, **329**, 163.

11 (*a*) S. Sarkar, F. S. T. Khan, T. Guchhait and S. P. Rath, Binuclear Complexes with Single M-F-M Bridge (M: Fe, Mn, and Cu): A Critical Analysis of the Impact of Fluoride for Isoelectronic Hydroxide Substitution, *Coord. Chem. Rev.*, 2023, **479**, 215003; (*b*) D. Lai, F. S. T. Khan and S. P. Rath, Multiheme proteins: Effect of heme–heme interactions, *Dalton Trans.*, 2018, **47**, 14388; (*c*) F. S. T. Khan, T. Guchhait, S. Sasmal and S. P. Rath, Hydroxo-bridged diiron(III) and dimanganese(III) bisporphyrins: modulation of metal spins by counter anions, *Dalton Trans.*, 2017, **46**, 1012; (*d*) D. Sil and S. P. Rath, An Ethane-bridged Porphyrin Dimer as Model of Di-heme Proteins: Inorganic and Bioinorganic Perspectives and Consequences of Heme-Heme Interactions, *Dalton Trans.*, 2015, **44**, 16195.

12 (*a*) F. S. T. Khan, A. K. Pandey and S. P. Rath, Remarkable anion- dependent spin-state switching in diiron(III)-μ-hydroxo bisporphyrins: What role do counterions play?, *Chem. – Eur. J.*, 2016, **22**, 16124; (*b*) D. Sil, F. S. T. Khan and S. P. Rath, Effect of inter-porphyrin distance on spin-state in diiron(III) μ-hydroxo bisporphyrins, *Chem. – Eur. J.*, 2016, **22**, 14585; (*c*) S. K. Ghosh, S. Bhowmik, D. Sil and S. P. Rath, Effect of heme-heme interactions and modulation of metal spins by counter anions in a series of diiron(III)-μ-hydroxo bisporphyrins: Unusual stabilization of two different spins in a single molecular framework, *Chem. – Eur. J.*, 2013, **19**, 17846; (*d*) M. A. Sainna, D. Sil, D. Sahoo, B. Martin, S. P. Rath, P. Comba and S. P. de Visser, Spin-state ordering in hydroxo-bridged diiron(III)bisporphyrin complexes, *Inorg. Chem.*, 2015, **54**, 1919; (*e*) S. K. Ghosh and S. P. Rath, A remarkably bent diiron(III)-μ-hydroxo bisporphyrin: unusual stabilization of two spin states of iron in a single molecular framework, *J. Am. Chem. Soc.*, 2010, **132**, 17983.

13 S. K. Ghosh, R. Patra and S. P. Rath, Synthesis, structure and photocatalytic activity of a remarkably bent, cofacial ethene-linked diiron(III) μ-oxobisporphyrin, *Inorg. Chim. Acta*, 2010, **363**, 2791.

14 T. E. Clement, D. J. Nurco and K. M. Smith, Synthesis and characterization of a series of monometallo-, bimetallo-, and heterobimetallo-1, 2-ethene-linked cofacial bisporphyrins, *Inorg. Chem.*, 1998, **37**, 1150.

15 (*a*) K. M. Kadish, M. Autret, Z. Ou, P. Tagliatesta, T. Boschi and V. Fares, Synthesis, structure, and electrochemistry of an electron deficient μ-oxo porphyrin dimer, $[(TPPBr_4)Fe]_2O$, *Inorg. Chem.*, 1997, **36**, 204; (*b*) A. L. Balch, L. Latos-Grażyński and T. N. St. Claire, Chemistry of iron oxophlorins. 3. reversible, one-electron oxidation of the iron(III) octaethyloxophlorin dimer, *Inorg. Chem.*, 1995, **34**, 1395; (*c*) L. A. Bottomley, J.-N. Gorce and J. T. Landrum, Spectroelectrochemistry of a urea-linked oxo-bridged iron-porphyrin dimer, *Inorg. Chim. Acta*, 1986, **125**, 135; (*d*) D. Chang, P. Cocolios, Y. T. Wu and K. M. Kadish, The four-electron oxidation of a novel μ-oxo dimer, $[((p\text{-}Et_2N)TPP)Fe]_2O$, *Inorg. Chem.*, 1984, **23**, 1629; (*e*) M. A. Phillippi and H. M. Goff, Electrochemical synthesis and characterization of the single-electron oxidation products of ferric porphyrins, *J. Am. Chem. Soc.*, 1982, **104**, 6026.

16 (*a*) T. Li, J. Neal, G. R. A. Wyllie, C. E. Schulz and W. R. Scheidt, Structural and magnetic effects of *meso*-substitution in alkyl-substituted metalloporphyrinate π-cation radicals: Characterization of $[Fe(TalkylP^{\bullet})(Cl)]SbCl_6$ (alkyl=ethyl and *n*-propyl), *Inorg. Chem.*, 2010, **49**, 8078; (*b*) S. Hu and T. G. Spiro, The origin of infrared marker bands of porphyrin π-cation radicals: Infrared assignments for cations of copper(II) complexes of octaethylporphine and tetraphenylporphine, *J. Am. Chem. Soc.*, 1993, **115**, 12029.

17 B. Cheng, J. D. Hobbs, P. G. Debrunner, J. Erlebacher, J. A. Shelnutt and W. R. Scheidt, An unusual near-eclipsed porphyrin ring orientation in two crystalline forms of (μ-oxo) bis[(octaethylporphinato)iron(III)]. Structural and molecular mechanics studies, *Inorg. Chem.*, 1995, **34**, 102.

18 J. A. Shelnutt, Molecular simulations and normal-coordinate structural analysis of porphyrins and heme proteins, in *The Porphyrin Handbook*, ed. K. M. Kadish, K. M. Smith and R. Guilard, Academic Press, New York, 2000, vol. 7, p. 167.

19 M. O. Senge, S. A. MacGowan and J. M. O'Brienb, Conformational control of cofacotrs in nature-the influence of protein-induced macrocycle distortion on the bio-

logical function of tetrapyrroles, *Chem. Commun.*, 2015, **51**, 17031.

20 (*a*) R. Weiss, A. Gold and J. Terner, Cytochromes *c*′: Biological models for the *S*=3/2, 5/2 spin-state admixture?, *Chem. Rev.*, 2006, **106**, 2550; (*b*) Y. Ling and Y. Zhang, Mössbauer, NMR, geometric, and electronic properties in *S* = 3/2 iron porphyrins, *J. Am. Chem. Soc.*, 2009, **131**, 6386; (*c*) D. Sakow, D. Baabe, B. Böker, O. Burghaus, M. Funk, C. Kleeberg, D. Menzel, C. Pietzonka and M. Bröring, Iron 10-thiacorroles: Bioinspired iron(III) complexes with an intermediate spin (*S*=3/2) ground state, *Chem. – Eur. J.*, 2014, **20**, 2913.

21 W. R. Scheidt, Systematics of the stereochemistry of porphyrins and metalloporphyrins, in *The Porphyrin Handbook*, ed. K. M. Kadish, K. M. Smith and R. Guilard, Academic Press, New York, 2000, vol. 7, p. 49.

22 (*a*) D. Sahoo, M. G. Quesne, S. P. de Visser and S. P. Rath, Hydrogen-bonding interactions trigger a spin-flip in iron (III) porphyrin complexes, *Angew. Chem., Int. Ed.*, 2015, **54**, 4796; (*b*) P. Chakraborty, N. Ghosh, N. Awasthi and S. P. Rath, Spin-flip *via* subtle electronic perturbation in axially ligated diiron(III) porphyrin dimer, *Chem. – Eur. J.*, 2024, **30**, e202400266; (*c*) D. Sahoo and S. P. Rath, Controlled generation of highly saddled (porphyrinato) iron(III) iodide, tri-iodide and one-electron oxidized complex, *Chem. Commun.*, 2015, **51**, 16790.

23 (*a*) M. Nakamura, Electronic structures of highly deformed iron(III) porphyrin complexes, *Coord. Chem. Rev.*, 2006, **250**, 2271; (*b*) A. Ikezaki, Y. Ohgo and M. Nakamura, NMR studies on the electronic structure of one-electron oxidized complexes of iron(III) porphyrinates, *Coord. Chem. Rev.*, 2009, **253**, 2056.

24 (*a*) I. Bertini, C. Luchinat, G. Parigi and E. Ravera, in *NMR of Paramagnetic Molecules*, Elsevier, Amsterdam, 2nd edn, 2017; (*b*) F. A. Walker, Proton NMR and EPR spectroscopy of paramagnetic metalloporphyrins and heme proteins, in *Handbook of Porphyrin Science*, ed. K. M. Kadish, K. M. Smith and R. Guilard, World Scientific, Singapore, 2010, vol. 6, p. 1.

25 H. Kalish, J. E. Camp, M. StÈ©pień, L. Latos-Grażyński, M. M. Olmstead and A. L. Balch, *meso* Substituent effects on the geometric and electronic structures of high-spin and low-spin iron(III) complexes of mono-*meso*-substituted octaethylporphyrins, *Inorg. Chem.*, 2002, **41**, 989.

26 M. Barfield and P. Fagerness, Density functional theory/GIAO studies of the ^{13}C, ^{15}N, and ^{1}H NMR chemical shifts in aminopyrimidines and aminobenzenes: Relationships to electron densities and amine group orientations, *J. Am. Chem. Soc.*, 1997, **119**, 8699.

27 M. Fizer, M. Slivka, N. Korol and O. Fizer, Identifying and explaining the regioselectivity of alkylation of 1,2,4-triazole-3-thiones using NMR, GIAO and DFT methods, *J. Mol. Struct.*, 2021, **1223**, 128973.

28 G. N. LaMar and F. A. Walker, *Porphyrins*, 1979, **4**, 61.

29 H. M. McConnell and R. E. Robertson, Isotropic nuclear resonance shifts, *J. Chem. Phys.*, 1958, **29**, 1361.

30 E. D. Hedegård, J. Kongsted and S. P. Sauer, Validating and analyzing EPR hyperfine coupling constants with density functional theory, *J. Chem. Theory Comput.*, 2013, **9**, 2380.

31 R. K. Tiwari, R. Nabi, R. L. Kumawat, B. Pathak and G. Rajaraman, Enhancing spin-transport characteristics, spin-filtering efficiency, and negative differential resistance in exchange-coupled dinuclear Co(II) complexes for molecular spintronics applications, *Inorg. Chem.*, 2023, **63**, 316.

32 C. Duboc, D. Ganyushin, K. Sivalingam, M.-N. Collomb and F. Neese, Systematic theoretical study of the zero-field splittinng in coordination complexes of Mn(III). Density functional theory versus multireference wave function approaches, *J. Phys. Chem. A*, 2010, **114**, 10750.

33 W. Kohn, A. D. Becke and R. G. Parr, Density functional theory of electronic structure, *J. Phys. Chem.*, 1996, **100**, 12974.

34 M. Frisch, G. Trucks, H. Schlegel, G. Scuseria, M. Robb, J. Cheeseman, G. Scalmani, V. Barone, G. Petersson and H. Nakatsuji, *Gaussian 16, Revision C. 01*, Gaussian, Inc., Wallingford CT, 2016.

35 J. Tirado-Rives and W. L. Jorgensen, Performance of B3LYP density functional methods for a large set of organic molecules, *J. Chem. Theory Comput.*, 2008, **4**, 297.

36 F. Weigend and R. Ahlrichs, Balanced basis sets of split valence, triple zeta valence and quadruple zeta valence quality for H to Rn: Design and assesment of accuracy, *Phys. Chem. Chem. Phys.*, 2005, **7**, 3297.

37 S. K. Singh and G. Rajaraman, Can anisotropic exchange be reliably calculated using density functional methods? A case study on trinuclear MnIII-MIII-MnIII (M=Fe, Ru, and Os) cyanometalate single-molecule magnets, *Chem. – Eur. J.*, 2014, **20**, 113.

38 N. Berg, T. N. Hooper, J. Liu, C. C. Beedle, S. K. Singh, G. Rajaraman, S. Piligkos, S. Hill, E. K. Brechin and L. F. Jones, Synthetic, structural, spectroscopic and theoretical study of a Mn(III)-Cu(II) dimer containing a Jahn-Teller compressed Mn ion, *Dalton Trans.*, 2013, **42**, 207.

39 A. E. Dearle, D. J. Cutler, H. W. Fraser, S. Sanz, E. Lee, S. Dey, I. F. Diaz-Ortega, G. S. Nichol, H. Nojiri and M. Evangelisti, An $[FeIII_{34}]$ molecular metal oxide, *Angew. Chem., Int. Ed.*, 2019, **58**, 16903.

40 B. Vranovičová and R. Boča, Magnetostructural J-correlations in Fe(III) complexes-A revision, *Nova Biotechnol. Chim.*, 2013, **12**, 70.

41 N. F. Chilton, R. P. Anderson, L. D. Turner, A. Soncini and K. S. Murray, PHI: A powerful new program for the analysis of anisotropic monomeric and exchange-coupled polynuclear *d*- and *f*-block complexes, *J. Comput. Chem.*, 2013, **34**, 1164.

42 T. Rajeshkumar, H. V. Annadata, M. Evangelisti, S. K. Langley, N. F. Chilton, K. S. Murray and G. Rajaraman, Theoretical Studies on Polynuclear $\{CuII_5GdIII_n\}$ Clusters (n = 4, 2): Towards Understanding Their Large Magnetocaloric Effect, *Inorg. Chem.*, 2015, **54**, 1661.

